Scalable Core–Shell MoS$_2$/Sb$_2$Se$_3$ Nanorod Array Photocathodes for Enhanced Photoelectrochemical Water Splitting

Liping Guo, Pravin S. Shinde, Yanxiao Ma, Lin Li, Shanlin Pan,* and Feng Yan*

Photoelectrochemical (PEC) hydrogen generation is a promising solar energy harvesting technique to address the concerns about the ongoing energy crisis. Antimony selenide (Sb$_2$Se$_3$) with van der Waals-bonded quasi-1D (Q1D) nanoribbons, for instance, (Sb$_4$Se$_6$)$_m$, has attracted considerable interest as a light absorber with Earth-abundant elements, suitable bandgap, and a desired sunlight absorption coefficient. By tuning its anisotropic growth behavior, it is possible to achieve Sb$_2$Se$_3$ films with nanostructured morphologies that can improve the light absorption and photogenerated charge carrier separation, eventually boosting the PEC water-splitting performance. Herein, high-quality Sb$_2$Se$_3$ films with nanorod (NR) array surface morphologies are synthesized by a low-cost, high-yield, and scalable close-spaced sublimation technique. By sputtering a nonprecious and scalable crystalline molybdenum sulfide (MoS$_2$) film as a cocatalyst and a protective layer on Sb$_2$Se$_3$ NR arrays, the fabricated core–shell structured MoS$_2$/Sb$_2$Se$_3$ NR PEC devices can achieve a photocurrent density as high as -10 mA cm^{-2} at 0 V$_{RHE}$ in a buffered near-neutral solution (pH 6.5) under a standard simulated air mass 1.5 solar illumination. The scalable manufacturing of nanostructured MoS$_2$/Sb$_2$Se$_3$ NR array thin-film photocathode electrodes for efficient PEC water splitting to generate solar fuel is demonstrated.

1. Introduction

Solar energy conversion technologies promise a renewable, sustainable, and affordable way of addressing the energy crisis due to depleting fossil fuel sources. The photovoltaic effect-based solar cell is one of the best examples of effective solar energy harvesting, a most successful commercial application.[1] However, to continuously store the photogenerated energy is still a great challenge to utilize solar energy sustainably. Photoelectrochemical (PEC) solar water splitting to generate oxygen through water oxidation and evolution of hydrogen (H$_2$) as an energy carrier is an attractive technique that combines solar energy harvesting and water electrolysis in a single device.[2] It is demonstrated that the water oxidation is the most difficult reaction during water splitting.[3] As a light-harvesting material, the semiconducting absorber is desired to have a suitable bandgap (e.g., 1.0–2.0 eV)[4] to utilize and absorb a significant portion of sunlight. While serving as electrode material in an electrolyzer, the absorber should have a low over-potential for hydrogen evolution reaction (HER, $2H^+ + 2e^- \rightarrow H_2$) to efficiently reduce the hydrogen ions to H$_2$.[5,6] Thus, to explore the Earth-abundant and inexpensive photoelectrodes and HER catalysts for PEC applications is of great interest for cost-effective solar energy conversion and storage applications.[7,8] For example, a considerable number of oxides such as Fe$_2$O$_3$, Cu$_2$O, TiO$_2$, and BiVO$_4$ and the chalcogenides such as Cu(In, Ga) S$_2$, Cu$_2$ZnSnS$_4$, CdTe, and SnS have been intensely investigated as PEC absorbers.[9–15]

Recently, the antimony selenide (Sb$_2$Se$_3$) chalcogenide has emerged as a promising light absorber material for photovoltaic devices whose power conversion efficiency (PCE) reaches as high as $\approx$9.2%.[16] The high optical absorption coefficient ($>10^5$ cm^{-3}), ideal low bandgap ($\approx$1.2 eV), low toxicity, high stability, and abundance in Earth make Sb$_2$Se$_3$ a promising candidate in PEC devices.[4,17–20] Sb$_2$Se$_3$ is also popularly known as a quasi-1D (Q1D) material with an anisotropic orthorhombic structure, which can assist the transport of photoexcited carriers along the oriented (Sb$_4$Se$_6$)$_n$ ribbons.[21] Nanostructured Sb$_2$Se$_3$ is reported to achieve a decent PEC hydrogen generation performance in the forms of nanoneedles, nanowires, and nanoarrays.[22–26] These nanostructures could efficiently elevate the electrical and optical properties due to improved light absorption and charge carrier transportation.[26] Furthermore, to realize the scalability of PEC applications, Sb$_2$Se$_3$ polycrystalline thin-film photocathodes have been investigated. The best stable PEC performance is reported in a benign neutral electrolyte (pH $\approx$ 6.5)

L. Guo, Prof. L. Li, Prof. F. Yan
Department of Metallurgical and Materials Engineering
University of Alabama
Tuscaloosa, AL 35487, USA
E-mail: fyan@eng.ua.edu

Dr. P. S. Shinde, Dr. Y. Ma, Prof. S. Pan
Department of Chemistry and Biochemistry
University of Alabama
Tuscaloosa, AL 35487, USA
E-mail: span1@ua.edu

Prof. F. Yan
Alabama Water Institute
University of Alabama
Tuscaloosa, AL 35487, USA

for thermally evaporated Sb_2Se_3 film in a *p*–*n* junction substrate configuration by coupling with an n-type CdS/TiO_2 followed by the use of expensive Pt coating as the cocatalyst on the surface that exhibits a photocurrent density of -8.6 mA cm^{-2} at 0 V versus reversible hydrogen electrode (V_{RHE}).[4] Recently, the solution-processed Sb_2Se_3 photocathodes achieved -11 mA cm^{-2} at 0 V versus reversible hydrogen electrode in the near-neutral electrolytes.[19] In a strongly acidic electrolyte (1 M H_2SO_4, pH ≈ 1), Sb_2Se_3 thin film prepared with the selenization of electrodeposited Sb and Pt cocatalyst further improves the photocurrent density to 16 mA cm^{-2} at 0 V_{RHE}.[27] By introducing a Cu-doped NiO_x hole-selective layer as an effective bottom contact layer for a solution-processed Sb_2Se_3 photocathode, a record photocurrent density of 17.5 mA cm^{-2} at 0 V_{RHE} in acidic electrolytes is achieved.[28]

Although Sb_2Se_3 photocathodes were reported as intrinsically stable toward photocorrosion in acidic electrolytes (pH ≈ 1), to achieve high stability, anti-photocorrosion layers were widely applied.[27] Among all the stable performances reported so far, Sb_2Se_3 has been protected by precious metal cocatalysts such as Pt or RuO_x and high bandgap oxides, e.g., TiO_2, to avoid the inevitable photocorrosion.[3,29] Therefore, the use of inexpensive protective materials or catalysts is in high demand, to be suitable for scalable manufacturing. Few efforts have been directed toward using the nonprecious cocatalysts such as transition metal dichalcogenides (TMDs) to improve the PEC hydrogen generation further and avoid the photocorrosion of Sb_2Se_3.[26,30–32] Molybdenum sulfide (MoS_2), one of the TMDs, is a typical 2D layered material and has promising properties for HER such as a suitable band alignment and good chemical as well as photocorrosion stability.[30,33,34] Recently, we have shown that the ≈30–40 nm crystalline MoS_2 layer on the Cu_2O photocathode solves the photocorrosion issue with dramatic improvement in photocurrent.[34] A solution-based approach of synthesizing amorphous/crystalline MoS_2 has been used to protect several photocatalysts, including Cu_2O, Sb_2S_3, and Sb_2Se_3.[27,34,35] However, the solution-processed MoS_x catalyst faces various issues, including thickness uniformity, composition dependence of the synthetic procedure, and scalability.[2] In contrast, the physical vapor deposition (PVD) techniques such as sputtering offer a better way to synthesize stable, uniform, and large-area MoS_2 thin films with great control.[36,37] However, minimal efforts have been made to synthesize the large-scale MoS_2 heterostructures by PVD techniques and use them for photocatalysis applications.

Herein, we present an efficient polycrystalline Sb_2Se_3 thin-film photocathode with a nanostructured surface and MoS_2 catalytic layer for PEC water splitting. This Sb_2Se_3 photocathode has been fabricated with a relatively unexplored close-spaced sublimation (CSS) method. CSS is a low-cost and high-yield method commonly used in solar cell fabrication, such as CdTe thin-film solar cells, as shown by our recent study.[38] The fast deposition rate of 1 μm min^{-1} can be achieved with CSS to fabricate numerous compound semiconductors. We have successfully fabricated high-quality Sb_2Se_3 thin films using the CSS technique for thin-film solar cell applications with PCE ≈7%.[17,39,40] Here, we tailor the CSS growth condition to grow Sb_2Se_3 nanorod (NR) arrays on top of the Sb_2Se_3 film simultaneously during deposition to increase light absorption and scattering. Using a scalable

sputtered MoS_2 catalyst to protect the CSS-grown Sb_2Se_3 NR arrays, a stable photocurrent density of -10 mA cm^{-2} at 0 V_{RHE} has been demonstrated in a near-neutral electrolyte (pH ≈ 6.5), which exhibits one of the highest PEC performances reported for the Sb_2Se_3 film-based photocathodes without using expensive Pt catalyst.

2. Results and Discussion

As shown in **Figure 1**a, the Sb_2Se_3 thin films were deposited using a CSS method, where the pure Sb_2Se_3 powder was sublimated at a high temperature in a short time and was deposited onto the fluorine-doped tin oxide (FTO) substrate. The CSS growth rate can reach ≈1 μm min^{-1}, which is suitable for large-scale manufacturing.[17] The top-view surface and cross-sectional topographies of the as-grown Sb_2Se_3 film were examined using scanning electron microscopy (SEM) (Figure 1d,e). The Sb_2Se_3 film thickness is ≈1 μm, and the surface of the Sb_2Se_3 film is covered by the Sb_2Se_3 NR arrays (≈200 nm in diameter and length ≈1000 nm), which is associated with the fast CSS growth rate of its orthorhombic structure. The CSS-deposited NR-structured Sb_2Se_3 film shows a texture behavior with preferred growth direction (confirmed in the X-ray diffraction [XRD] results later). The cross-sectional view of as-grown Sb_2Se_3 reveals uniform and dense films without any voids at the interface of Sb_2Se_3/FTO, indicating the better adhesiveness of noncubic Sb_2Se_3 on transparent conducting oxides (TCOs) than that of cubic chalcogenides (Figure 1g) such as CdTe (see Supporting Information).[41] Sb_2Se_3 was then introduced to a high-vacuum radio frequency (RF) sputtering system for MoS_2 deposition (Figure 1b). Figure 1f shows that the Sb_2Se_3 film still preserves its NR structure after being coated with 30 nm MoS_2. The corresponding cross-sectional SEM image (Figure 1g) shows that the MoS_2 layer entirely covers the Sb_2Se_3 NRs and exhibits core–shell structures of MoS_2/Sb_2Se_3 NRs. We anticipate an improved PEC performance with such core–shell MoS_2/Sb_2Se_3 NR arrays on the Sb_2Se_3 films because of the increased surface area and NR structures enabling enhanced light absorption via light scattering and localization (Figure 1c).

To ascertain the coverage of the 30 nm-thick sputtered MoS_2 on the Sb_2Se_3 film and the Sb_2Se_3 NR surfaces, we used the SEM equipped with energy-dispersive X-ray spectroscopy (EDS) to identify the core–shell structured MoS_2/Sb_2Se_3 NR arrays in detail. As shown in **Figure 2**a, the CSS-deposited Sb_2Se_3 film has no visible physical defects in the bulk of the film, and the sputtered MoS_2 coating is uniformly distributed on top of the Sb_2Se_3 film to have the completely covered core–shell NR structure. The morphology of the sputtered MoS_2 film on the FTO substrate exhibits a granular structure (see Figure S1, Supporting Information). The magnified image of the NR arrays (Figure 2b) reveals the full coverage of MoS_2 on the Sb_2Se_3 NR. The elemental SEM–EDS mapping of Sb, Se, Mo, and S shows that the Se content is weak on the surface, whereas the Sb exhibits a strong signal on the surface, but the Sb mapping is smaller than that of Mo and S. This elemental spatial distribution feature confirms that the MoS_2/Sb_2Se_3 core–shell NR structure is formed with the help of sputtered MoS_2. Moreover, the uniform
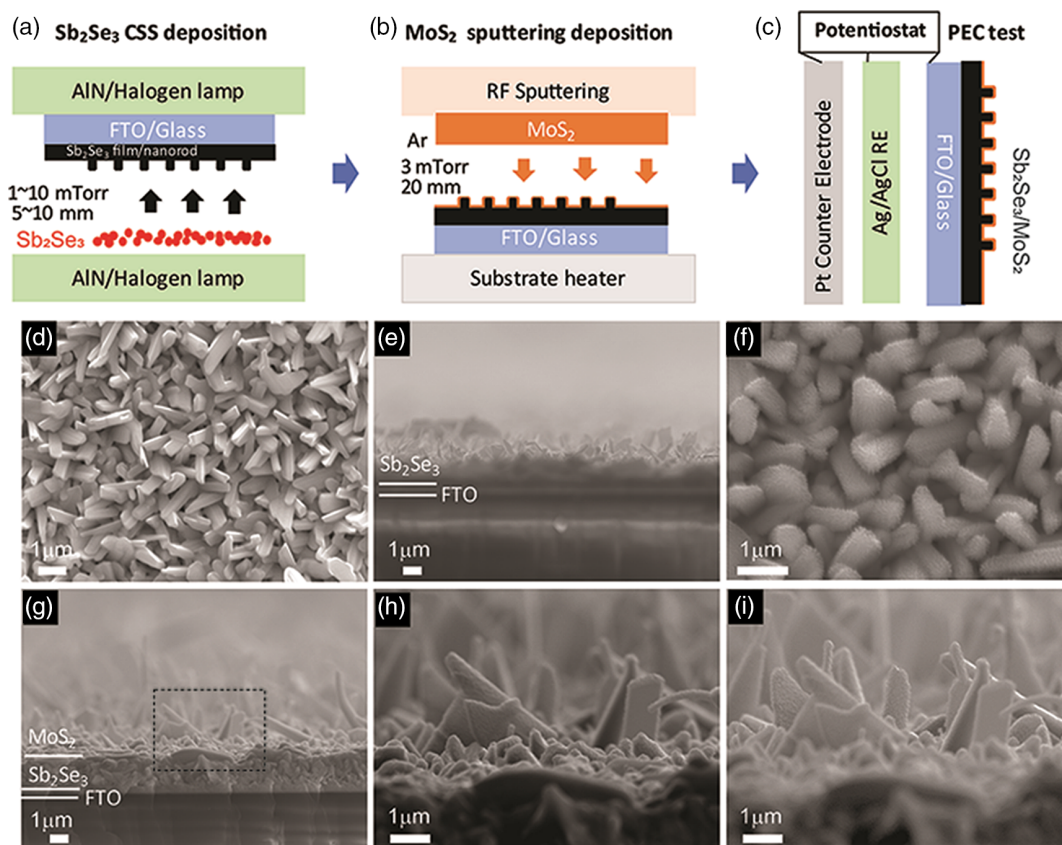
Figure 1. Schematics showing a) the fabrication process of CSS-deposited Sb_2Se_3 thin films, b) synthesis of MoS_2 thin film by sputtering, and c) PEC measurement setup for core–shell MoS_2/Sb_2Se_3 NR array electrodes. d) Top-view and e) cross-sectional SEM images of CSS-deposited Sb_2Se_3 revealing surface morphology and film thickness. f) Top-view and g) cross-sectional SEM images of the as-grown MoS_2/Sb_2Se_3 NR electrode. h,i) Magnified images of the MoS_2/Sb_2Se_3 NRs on the Sb_2Se_3 film as marked in (g) with different work distances.

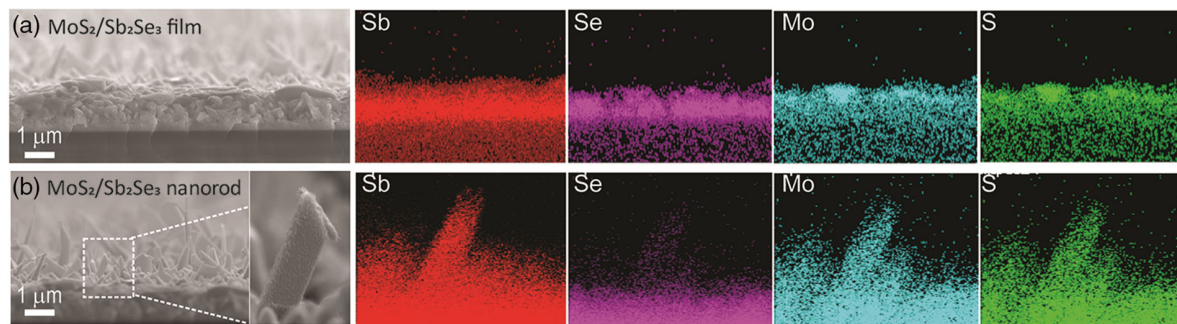**Figure 2.** MoS_2/Sb_2Se_3 core–shell NR characterization. Cross-sectional SEM side view of MoS_2/Sb_2Se_3 revealing the a) film side and b) MoS_2/Sb_2Se_3 core–shell NR array with the corresponding EDS elemental mapping images of constituent elements.

and full coverage of MoS_2 coating indicates well adhesion and proper heterojunction formation between the sputtered MoS_2 shell and Sb_2Se_3 NR array core. The rough surface of MoS_2 could also benefit HER due to the more facet and active sites.[42]

To determine the coverage of the sputtered MoS_2 shell layer grown on the Sb_2Se_3 NR surface and the junction interface elemental distribution, transmission electron microscopy (TEM) and high-angle annular dark-field scanning transmission

electron microscopy (HAADF-STEM) with attached EDS were used to characterize the MoS_2/Sb_2Se_3 core–shell NR and inter-face. As shown in **Figure 3**a,b, the sputtered MoS_2 was uniformly coated on the Sb_2Se_3 NR and formed a core–shell structure. Notably, the sputtered MoS_2 layer (≈30 nm thickness) contains remarkable nanocrystalline particles (≈10 nm). This morphology of the accumulated MoS_2 structure exists not only on the Sb_2Se_3 NR but also segregates among the valleys between the NRs and
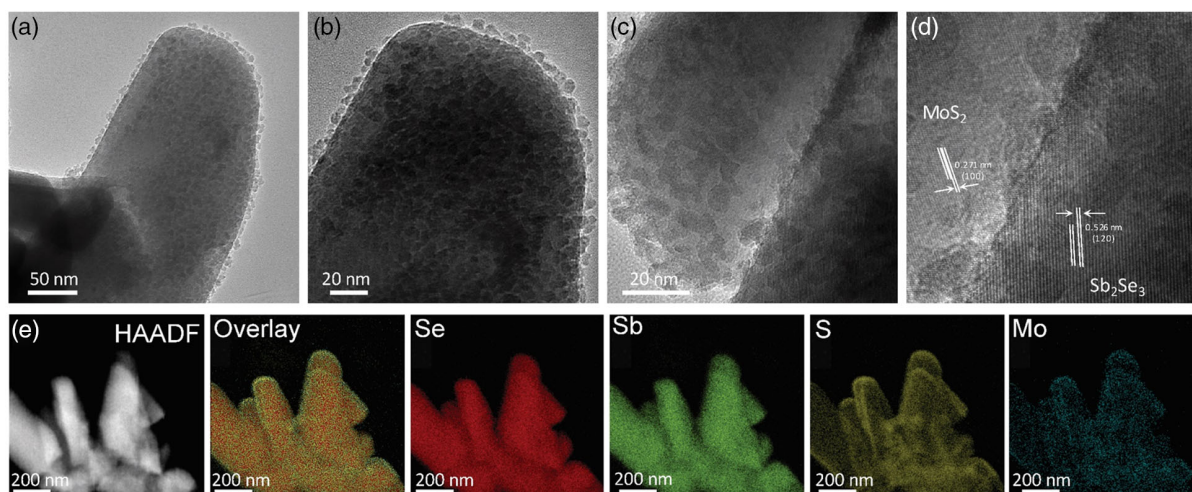
Figure 3. Characterization of MoS_2/Sb_2Se_3 core–shell NR junction interface. a) HAADF-STEM image and EDS elemental mapping with Sb, Se, S, and Mo; b,c) TEM image of the MoS_2/Sb_2Se_3 NR; and d,e) MoS_2/Sb_2Se_3 junction interface.

the bottom compact Sb_2Se_3 film. The MoS_2/Sb_2Se_3 interface is shown in Figure 3c,d with lattice fringes belonging to MoS_2 and Sb_2Se_3, respectively. The dense and uniform coverage of the sputtered MoS_2 shell layer promises excellent adhesion and decently defined junction formation between the Sb_2Se_3 NR and the MoS_2 layer. Figure 3e shows the Z-contrast HAADF MoS_2/Sb_2Se_3 NR with overlay, Se, Sb, S, and Mo elements distribution.

To ascertain the role of sputtered MoS_2 in inhibiting photocorrosion, we systematically characterized the optical and electrocatalytic performance of the pure MoS_2 layer as a function of thickness. **Figure 4**a shows the optical bandgap extracted from the transmittance of the bare Sb_2Se_3/FTO and MoS_2/FTO grown with various thicknesses. Sb_2Se_3 has a bandgap of $\approx 1.1\,eV$, whereas MoS_2 gradually shows a bandgap decrease with increasing thickness. The bandgap of the MoS_2 thin film changes from 2.56 eV for 20 nm to 1.67 eV for 50 nm. The optical image of the sputtered MoS_2 turns from light to dark brown with increasing thickness (Figure S2, Supporting Information), which corresponds to the optical bandgap change. Figure 4b shows the electrocatalytic behavior of the sputtered MoS_2 thin films of different thicknesses grown on the FTO substrate. The cyclic voltammetry (CV) measurements show that 30 nm-thick MoS_2 is desired to provide the highest catalytic current density. Figure 4b is replotted in Supporting Information to calculate the Tafel slopes (Figure S3, Supporting Information). A 30 nm-thick MoS_2 exhibits a lower overpotential compared with other thicknesses. HER activity can be expressed in terms of the lower Tafel slope from the polarization plots. The 30 nm-thick MoS_2 exhibited a lower Tafel slope of 56 mV dec^{-1}, which is comparable with the literature values.[43] The previous study also suggested that the ≈ 30 nm-thick spin-coated MoS_2 was enough to protect the cuprous oxide film and help catalyze the water-splitting reactions.[27] The inset of Figure 4b shows the atomic force microscopy (AFM) surface morphology of the 30 nm-thick MoS_2 with root mean square (RMS) roughness of ≈ 5 nm, and the MoS_2 crystalline size is ≈ 100 nm.

To elucidate the structural impacts on the PEC performance of the core–shell MoS_2/Sb_2Se_3 NR array, the structure of the CSS-grown Sb_2Se_3 and 30 nm MoS_2-coated Sb_2Se_3 was characterized using both XRD and Raman spectra. Figure 4c shows the XRD patterns of FTO, as-grown MoS_2, pristine Sb_2Se_3, and $MoS_2/$ Sb_2Se_3. The pristine Sb_2Se_3 shows an orthorhombic structure with a space group of *Pbnm* (JCPDS 15-0861) with no secondary phase.[17] The (120), (211), and (221) peaks are indexed, and the texture coefficient is calculated (see Figure S4, Supporting Information), which suggests that the CSS-deposited Sb_2Se_3 has a (221)-preferred orientation. This texture behavior indicates that the $(Sb_4Se_6)_n$ ribbons are oriented and grown normal to the FTO substrate with a 46.1° tilt angle.[17,44] The XRD pattern of the sputtered MoS_2 on the FTO substrate did not reveal any phase peaks due to a small film thickness of MoS_2 (≈ 20–50 nm), showing highly intense peaks of the polycrystalline FTO structure. The XRD pattern of MoS_2-coated Sb_2Se_3 shows little difference with that of the pristine Sb_2Se_3, suggesting that the small amount of MoS_2 coating does not alter the phase structure of Sb_2Se_3 despite covering homogeneously on the Sb_2Se_3 surface.

The Raman spectra for the sputtered MoS_2 film show two prominent bands, $E_{2g}^1 \approx 383\,cm^{-1}$ and $A_{1g} \approx 407\,cm^{-1}$, respectively, suggesting that the crystalline structure of MoS_2 was formed at room temperature (Figure 4d).[45] This is different from the previous report that amorphous MoS_2 was fabricated at room temperature by sputtering.[37] The difference may result from the sputtering deposition conditions. Also, the Raman spectrum of bare Sb_2Se_3 shows two characteristic peaks at 189 and 253 cm^{-1} corresponding to the vibrations associated with two Sb bonds (Sb—Se and Sb—Sb, respectively), which is the indication of good crystallinity and no impurities.[46] The Raman spectra of the core–shell MoS_2/Sb_2Se_3 shows the likely overlap between pure Sb_2Se_3 and MoS_2, although the Raman peak intensity was reduced for both MoS_2 and Sb_2Se_3 which could be due to the variation in polarizability in the core–shell structured MoS_2/Sb_2Se_3 NR arrays.
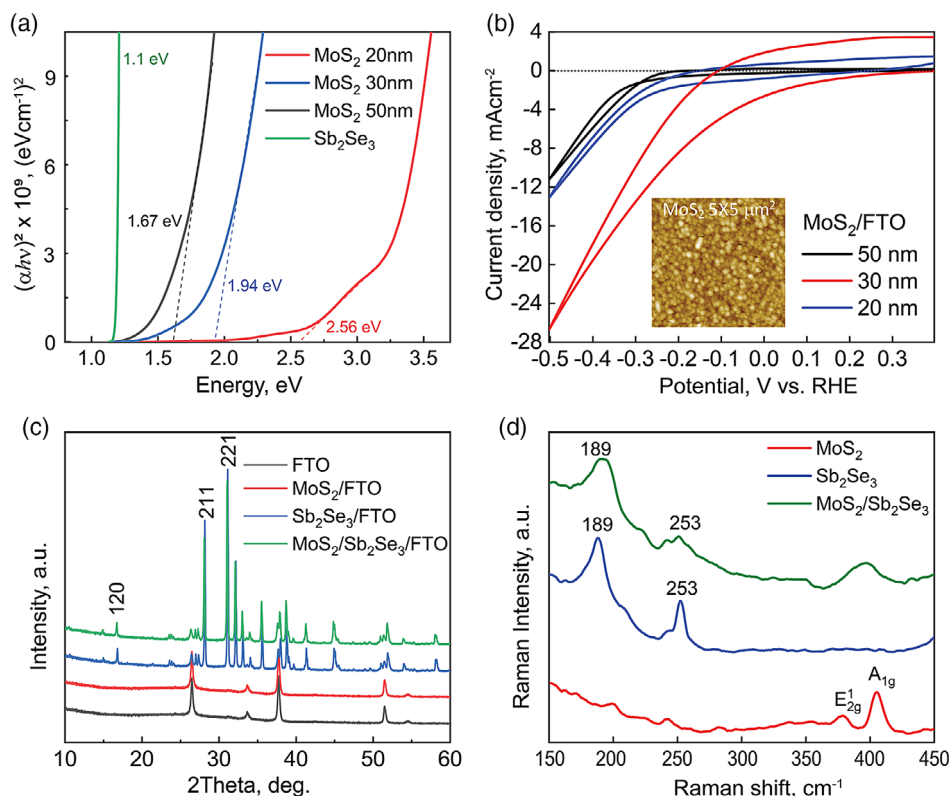
Figure 4. a) Tauc plots of sputtered MoS_2 layer with different thicknesses on FTO, b) polarization curves for HER performance of MoS_2 grown on FTO substrate. The inset shows the AFM of the sputtered MoS_2 (thickness ≈30 nm) with a smooth surface; c) XRD patterns of FTO, MoS_2, Sb_2Se_3, and MoS_2-coated Sb_2Se_3; and d) Raman spectra of sputtered MoS_2, Sb_2Se_3, and MoS_2-coated Sb_2Se_3.

To provide surface charge transport insights into the PEC device, we conducted the local electrostatic force microscopy (EFM) to determine its charge generation sites with high spatial resolution. Considering that the NR grew on the matrix of the Sb_2Se_3 film, as shown in **Figure 5**a, with the sputtered MoS_2 coating, we expected that the MoS_2/Sb_2Se_3 core–shell NR arrays distribute on top of Sb_2Se_3 films, as shown in Figure 5b. This unique hybrid nanostructure would help enhance the light absorption cross section and the populations of active sites for proton reduction reaction for solar water splitting. The NR structure would also

shorten the electron transport distance to reduce protons at the MoS_2–electrolyte interface while enabling efficient hole transport to the conductive substrate. Figure 5c shows the AFM images revealing the surface topography of a bare Sb_2Se_3 NR with its bottom embedded in the Sb_2Se_3 film matrix. The charge generation map in the EFM images shows that the charging rate varies across the surface of the film, with a spatial resolution better than 100 nm (see Figure S7, Supporting Information, for EFM details). The NR structure itself presents a low charge accumulation slower than that of the surrounding regions. This could be due to the
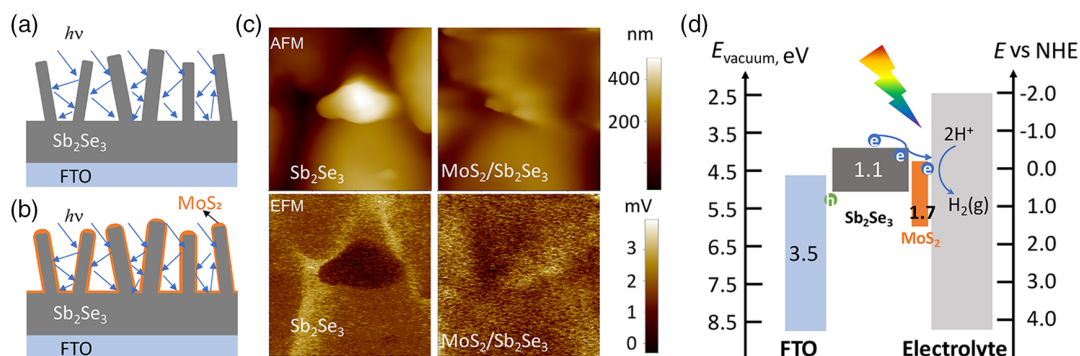

Figure 5. The schematic of a) Sb_2Se_3 NR/film and b) MoS_2/Sb_2Se_3 core–shell NR, showing the cross-sectional view of the core–shell NR structure, and c) the AFM topography (upper panels) and EFM (lower panels) images of the Sb_2Se_3 and MoS_2/Sb_2Se_3 NR (Area: 1.5 × 1.5 mm²). d) The band diagram for the FTO, Sb_2Se_3, MoS_2 at different energy scales, vacuum, and the normal hydrogen electrode (NHE).

lower charge concentration at the top of the NRs. By applying the sputtered MoS_2 layer, the AFM topography of the MoS_2/Sb_2Se_3 core–shell NR shows a smooth surface and uniform coverage. The EFM image of the core–shell MoS_2/Sb_2Se_3 NR shows a more uniform photogenerated charge distribution. It is believed that MoS_2 is helpful for charge transfer due to its larger work function (≈ 5.1 eV) than that of Sb_2Se_3 (≈ 4.6 eV). As shown in Figure 5d, the band diagram for the MoS_2/Sb_2Se_3 core–shell NR could also effectively split water and reduce H^+ into the hydrogen.

Figure 6 shows the PEC performance of the core–shell MoS_2/Sb_2Se_3 NR-based electrodes illuminated under air mass (AM) 1.5 G simulated sunlight. As shown in Figure 6a, the pristine Sb_2Se_3 NR array electrodes show catholic photocurrents under a linear voltammetry sweep from $+0.5$ to -0.2 V_{RHE}. Surprisingly, the CSS-deposited pristine Sb_2Se_3 film achieves a photocurrent of ≈ 4.2 mA cm^{-2} at 0 V_{RHE} during the first scan, which is much higher than the reported Sb_2Se_3 films fabricated by other deposition techniques. For example, the thermally evaporated pristine Sb_2Se_3 films show ≈ 10 µA cm^{-2}, whereas the solution-processed Sb_2Se_3 nanostructure displays ≈ 100 µA cm^{-2} at 0 V_{RHE}.[4,22] In addition, the PEC performance of Sb_2Se_3 film with NR arrays is also higher than that of pure nanostructured Sb_2Se_3 photocathodes. For example, Sb_2Se_3 nanoneedles with TiO_2 and Pt surface modification yields 2 mA cm^{-2} at 0 V_{RHE}.[25] Hence, CSS-deposited Sb_2Se_3 shows a significant photocurrent improvement for the pristine Sb_2Se_3 film with NR surface

structure, which suggests that CSS is suitable for high-quality Sb_2Se_3 production. However, with increasing the number of scans, the photocurrent decreased sharply to ≈ 1 mA cm^{-2} at 0 V_{RHE} (76% drop after the 3rd scan), which is also noticed for Sb_2Se_3 films prepared by other growth techniques. Nevertheless, the high PEC performance stems from the contribution of the Sb_2Se_3 NR structure surface, enabling efficient light absorption and short electron transport, although the film suffers from photocorrosion of the Sb_2Se_3 film surface. The photocorrosion is evidenced by the PEC product of the film, which is rich in Sb_2O_3, as shown in Figure S5, Supporting Information, X-ray photoelectron spectroscopy (XPS) data for Sb_2O_3 surface after PEC testing; the thickness of Sb_2O_3 is ≈ 2–3 nm.

To protect Sb_2Se_3 NRs from photocorrosion, a MoS_2 layer is sputtered onto the NR structure to prevent light-driven electrochemical oxidation while enhancing the selective proton reduction. It is expected that the MoS_2 can effectively protect the Sb_2Se_3 NR from direct contact with the 0.5 M Na_2SO_4 electrolyte. After 20 nm-thick MoS_2 coating, a significant improvement in photocurrent up to -8.0 mA cm^{-2} at 0 V_{RHE} was observed for the core–shell MoS_2/Sb_2Se_3 NR arrays during the first scan (Figure 6b). The improved photocurrent originates partially from the core–shell MoS_2/Sb_2Se_3 heterostructure formation to increase the light absorption range with a broad bandgap of MoS_2 and enhance the photogenerated carrier separation. However, with an increasing number of linear sweep voltammetry (LSV) scans, this core–shell MoS_2/Sb_2Se_3 still suffers from
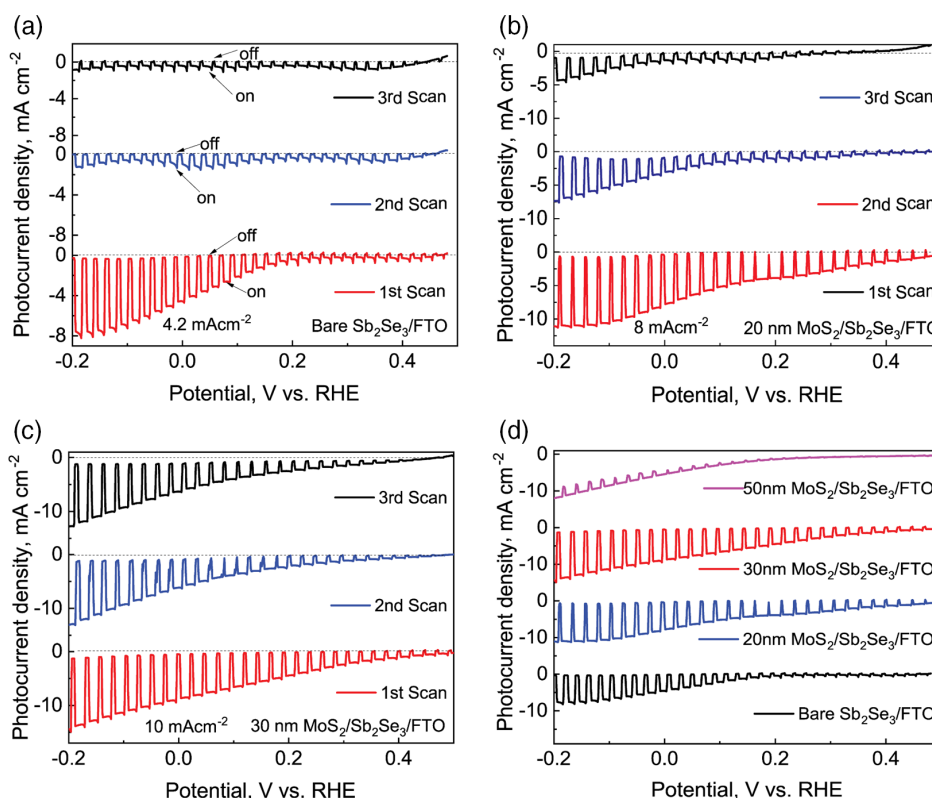

Figure 6. LSV of a) bare Sb_2Se_3, b) 20 nm, and c) 30 nm MoS_2-coated Sb_2Se_3 under intermittent 1 sun illumination pulses and the corresponding stability tests with three consecutive linear voltammetry scans. d) Shows the LSVs of bare Sb_2Se_3 and the ones coated with 20, 30, and 50 nm MoS_2 under intermittent 1 sun illumination.

corrosion, which indicates that 20 nm-thick MoS_2 is not sufficient to fully protect the Sb_2Se_3 NR arrays. The photocorrosion can stem from the grain boundary regimes between MoS_2 and Sb_2Se_3 NRs as the Sb_2Se_3 NR size is on the order of micrometer scale. A remarkable photocurrent enhancement up to $-10\,mA\,cm^{-2}$ at $0\,V_{RHE}$ is achieved with an increase in MoS_2 thickness to 30 nm (Figure 6c), which is stable for several LSV scans. This is on par with excellent photocurrent reported for Sb_2Se_3 photocathodes fabricated using other deposition techniques and more complicated PEC device structures, e.g., $-8.6\,mA\,cm^{-2}$ at $0\,V_{RHE}$ in $Sb_2Se_3/CdS/TiO_2/Pt$ structure at $pH \approx 6.5$.[4] However, with a further increase in the MoS_2 thickness to 50 nm (Figure 6d), the dark current dominates the PEC performance due to the thicker MoS_2 and may block the light absorption in Sb_2Se_3 (discussion later). This observation indicates that core–shell MoS_2/Sb_2Se_3 NR arrays are of high efficiency in water splitting as a photocathode. Moreover, the sputtered MoS_2 could be effective in protecting the Sb_2Se_3 NR and reduce the degradation for the Sb_2Se_3 NR array-based photocathodes.

To gain insights into the chemical states and stability during the photoactivity measurement, the core–shell structured MoS_2/Sb_2Se_3 NR array film was characterized using the EDS as well as XPS before and after the PEC test. **Figure 7**a–c shows the SEM with EDS spectra for the Sb_2Se_3, MoS_2/Sb_2Se_3 NR arrays before and after the PEC test, respectively. It is shown that the as-grown Sb_2Se_3 has a stoichiometric ratio between Sb and Se. With sputtered MoS_2 coating, the chemical composition of MoS_2 is close to 1:2, although it shows a slight overdose of S, which could be ascribed to the fact that S is easier to be sputtered due to its lighter weight. After the several scans of the PEC test (e.g., after the third scan), the pristine Sb_2Se_3 shows great degradation (Figure 6a), which could be due to the surface Sb_2O_3 that has dissolved (see Figure S5, Supporting Information, for XPS data), although there is no clear degradation mark in the optical image,

as shown in the inset of Figure 7a. Remarkably, the MoS_2/Sb_2Se_3 NR arrays are more stable (Figure 7b,c), and no discernible photocorrosion occurs on the MoS_2 shell on the Sb_2Se_3 NR arrays, as shown in the inset of Figure 7c (see Figure S6, Supporting Information, for more optical images). The stoichiometric ratio between Mo and S is slightly increased, which is good for photoactivity because it is reported that the photogenerated electrons are easier to transfer to the catalytically active S sites.[34,35] XPS spectra were further analyzed in detail to elucidate the structural variations of MoS_2-modified photocathode before and after the PEC test (Figure 7d–h). The XPS survey shows that the MoS_2 shell can effectively cover Sb_2Se_3 that led to the suppressed XPS intensity. When the XPS of MoS_2/Sb_2Se_3 NR arrays are compared before and after PEC measurement, the key observation is that $Sb3d_{5/2}$, $Se3d_{5/2}$, and $S2p_{3/2}$ show no shift in binding energy, but the XPS intensity is significantly increased. The variation in peak intensity suggests that Sb_2Se_3/MoS_2 interfacial diffusion occurs during the PEC test. This high-vacuum-sputtered MoS_2 behaves differently with the amorphous MoS_2 fabricated using the solution process due to the MoO_x surface oxides layer during solution process fabrication.[47] It was reported that the sulfurization of MoS_2–Sb_2Se_3 could lead to the partial conversion of surface Sb_2O_3 into Sb_2S_3 while keeping the Sb_2Se_3 unchanged.[27] Thus, the interfacial diffusion between Sb_2Se_3 and MoS_2 can contribute to the improved stability of the PEC performance. Here, the surface Sb_2O_3 on the CSS-deposited Sb_2Se_3 may also be sulfurized by MoS_2 during PEC, and the interfacial resistivity due to the existence of Sb_2O_3 can be decreased to benefit photoexcited charge transfer.

Figure 8a shows the linear sweep voltammograms recorded under chopped light illumination for as-grown Sb_2Se_3 and 30 nm-coated MoS_2/Sb_2Se_3 photocathodes. The current–voltage measurement suggests the occurrence of a recurring reduction peak at $\approx 0\,V$ versus RHE for the pristine Sb_2Se_3 electrode. Such behavior is due to the photocorrosion of Sb_2O_3 that undergoes
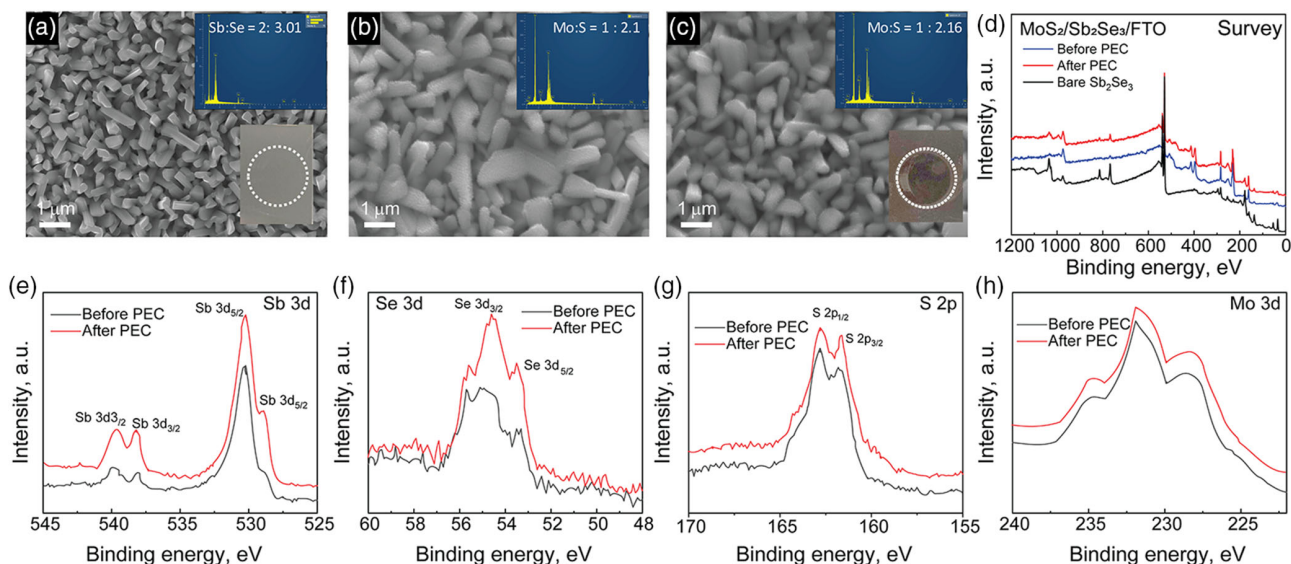

Figure 7. a–c) SEM images of the as-grown, Sb_2Se_3, MoS_2/Sb_2Se_3 before PEC, and MoS_2/Sb_2Se_3 after PEC measurement with inset showing the EDS spectra and digital photographs of the samples with dash line indexed the cell area, d–h) XPS spectra of MoS_2/Sb_2Se_3 before and after PEC test: d) survey, e), Sb 3d, f) Se 3d, g) Mo 3d, and h) S 2p.
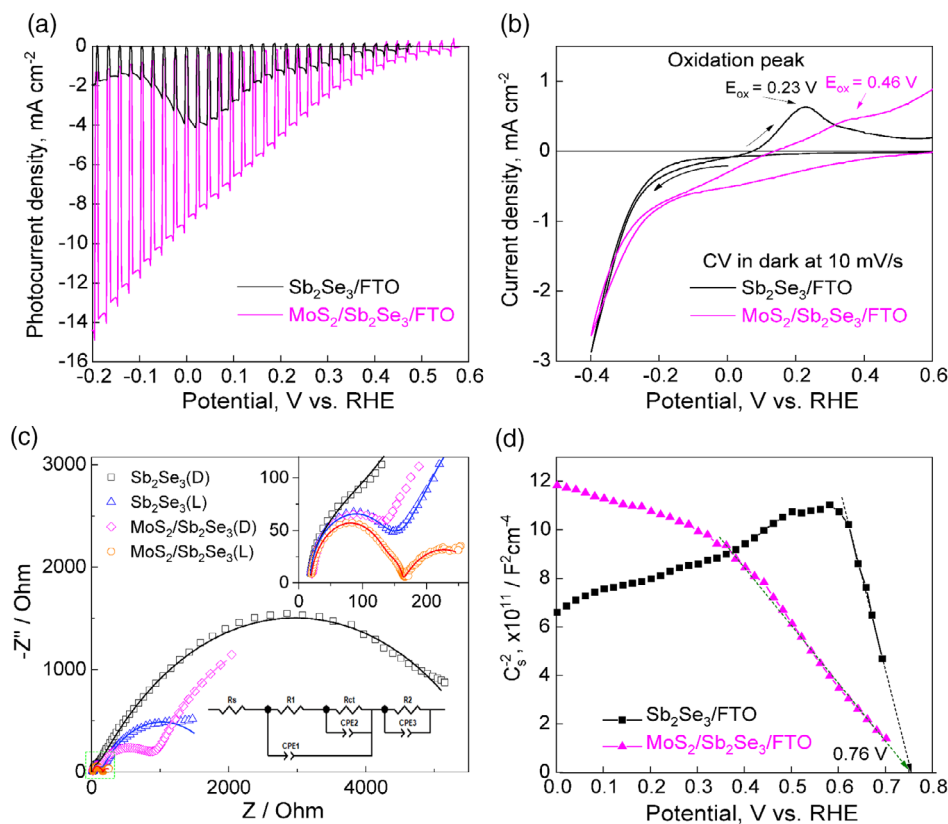
Figure 8. a) LSVs of bare Sb_2Se_3 and 30 nm MoS_2/Sb_2Se_3 photocathodes under intermittent AM 1.5 G simulated sunlight illumination. b) Cyclic voltammograms of pristine Sb_2Se_3 and MoS_2/Sb_2Se_3 photocathodes at 10 mV s^{-1}. c) Nyquist plots of Sb_2Se_3 and MoS_2/Sb_2Se_3 electrodes recorded at 0 V versus RHE (-0.6 V vs Ag/AgCl) both in the dark and under the light. The equivalent electrochemical circuit is used to fit the Nyquist plots, as shown in the inset. The discrete symbols and the solid lines represent the experimental and fitted data, respectively. Table 1 shows the electrochemical parameters obtained from the fitting d) M–S plots of pristine Sb_2Se_3 and MoS_2/Sb_2Se_3 electrodes measured at 1 kHz frequency in the dark. Electrolyte: 0.1 M phosphate-buffered 0.5 M Na_2SO_4 solution (pH 6.5); light source: simulated 1 sun (100 mW cm^{-2}).

reductive decomposition. No reduction peak appears for the MoS_2-protected Sb_2Se_3 sample. To realize the band alignment and protection of Sb_2Se_3 by MoS_2, the cyclic voltammograms of pristine Sb_2Se_3 and core–shell structured 30 nm MoS_2/Sb_2Se_3 were recorded at the scan rate of 10 mV s^{-1}. When CV is swept toward a negative direction, the onset potential of Sb_2Se_3 improves at least by 300 mV after its decoration by MoS_2. During reverse scan, pristine Sb_2Se_3 exhibits a prominent oxidation peak at 0.23 V, whereas a slight oxidation peak appears for MoS_2/Sb_2Se_3 at 0.46 V (Figure 8b). This confirms that MoS_2 protects Sb_2Se_3 from electrochemical corrosion. It is also remarkable to note that the MoS_2/Sb_2Se_3 heterojunction exhibits a higher onset potential (low overpotential) than that of pristine Sb_2Se_3, meaning that the onset potential of Sb_2Se_3 is improved upon passivation of MoS_2 layer. The improvement in onset potential (toward the anodic region) of the MoS_2/Sb_2Se_3 heterojunction photocathode suggests a higher photovoltage. Thus, the indication of significant improvement in the onset potential of Sb_2Se_3 suggests a small conduction band offset while forming a junction with MoS_2. In other words, MoS_2 and Sb_2Se_3 form a favorable band alignment or reduced band-energy mismatch, which is essential for efficient water-splitting reactions. To further evaluate the enhancement in photocurrent performance and

the increased onset potential, the electrochemical impedance spectroscopy (EIS) and Mott–Schottky (M–S) measurements are carried out to shed light on the charge transfer processes occurring at the electrolyte interface and obtain information about the nature and concentration of majority charge carriers in the Sb_2Se_3 photoelectrode before and after MoS_2 coating. Figure 8c shows the Nyquist plots of Sb_2Se_3 and MoS_2/Sb_2Se_3 electrodes obtained at ≈0.0 V versus RHE (-0.6 V Ag/AgCl) in the dark and under front-side illumination. The Nyquist curves were fitted using an equivalent electrochemical circuit (see inset of the figure) that comprised series resistance (R_s) and two or more resistance and capacitance in parallel (RC) circuits. R_s constitutes the sum of all the serial resistances consisting of the electrolyte, contact, conducting support, and electrical connections. For fitting the Nyquist plot of MoS_2/Sb_2Se_3, three RC circuits are used due to the additional interface of MoS_2. The charge transfer resistance (R_{ct}), which inversely dictates the photocurrent response by controlling the charge transport across the interface of the electrode surface and electrolyte, is decreased for Sb_2Se_3 after MoS_2 coating in both dark and light. A considerably lower R_{ct} value of 19.19 Ω is observed under illumination for thr MoS_2-protected Sb_2Se_3 electrode as against 1770.00 Ω for pristine Sb_2Se_3 (see **Table 1** for all the electrochemical

Table 1. Electrochemical parameters of photoelectrodes obtained from EIS study.

Samples/parameters	Pristine Sb_2Se_3		MoS_2/Sb_2Se_3	
	Dark	Light	Dark	Light
R_s [Ω]	18.32	18.24	20.20	18.58
R_1 [Ω]	98.76	128.70	118.00	124.10
CPE_1 [$\mu F\ cm^{-2}$]	0.1435	0.2437	0.2437	0.4821
R_{ct} [$F\ cm^{-2}$]	5765.00	1770.00	723.20	19.19
CPE_2 [$F\ cm^{-2}$]	28.7380	117.26	0.7104	22.6490
R_2 [Ω]	–	–	4428.00	130.60
CPE_3 [$F\ cm^{-2}$]	–	–	1386.90	12 494.00

CPE = constant phase element (meant for imperfect capacitance).

Figure 9. IPCE and integrated photocurrent density as a function of wavelength for MoS_2, Sb_2Se_3, and MoS_2-coated Sb_2Se_3 electrodes.

parameters). This implies that charge carrier resistance at the Sb_2Se_3–electrolyte interface is dramatically decreased. Thus, MoS_2 coating not only protects the surface of the Sb_2Se_3 electrode from photocorrosion but also facilitates the charge transfer properties at Sb_2Se_3, thereby actively improving the photocurrent response. A similar role of MoS_2 is reported for Cu_2O photocathodes.[34] The conduction behavior of the core–shell structured MoS_2/Sb_2Se_3 NR array was studied using the M–S plot (Figure 8d). The negative slopes of the M–S plots confirm the p-type semiconducting behavior of both as-grown Sb_2Se_3 and MoS_2/Sb_2Se_3 NR array electrodes. The flat band potential (E_{fb}) measured in 0.5 M Na_2SO_4 electrolyte is 0.76 ± 0.005 V for both the samples. E_{fb} is identical for both the electrodes, which indicates that the MoS_2 does not impact the conduction type of Sb_2Se_3, and also suggests that MoS_2 decoration protects the Sb_2Se_3 photocathode and the band bending is unaffected by it. Here, the CSS-deposited pristine Sb_2Se_3 and MoS_2/Sb_2Se_3 NR arrays have a higher E_{fb} value than that reported for the thermally evaporated Sb_2Se_3 film (e.g., 0.55 V).[36,48] The acceptor densities (see Supporting Information) estimated for pristine Sb_2Se_3 and MoS_2/Sb_2Se_3 are $\approx 2.0 \times 10^{16}$ and $5.6 \times 10^{16}\ cm^{-3}$, respectively. These values are one order of degree larger than that of the thermally evaporated Sb_2Se_3 (e.g., $1.14 \times 10^{15}\ cm^{-3}$).[36] The improved E_{fb} is associated with the enhanced heterojunction quality and increased doping density with the sputtered MoS_2 layer. However, the measured carrier density is much lower than that of the reported carrier density ($1 \times 10^{18}\ cm^{-3}$) in the electrodeposited Sb_2Se_3 film, which could be due to more dopants involved during electrodeposition.[30] This also indicates that the photocurrent improvement for the MoS_2/Sb_2Se_3 NR arrays is attributed to the increased carrier concentration.

Figure 9 shows the incident photon to current conversion efficiency (IPCE) spectra of MoS_2, Sb_2Se_3, and MoS_2-coated Sb_2Se_3 grown on the FTO substrate under monochromatic illumination. The Sb_2Se_3 photocathodes with 1.1 eV bandgap can harvest solar spectrum as high as 1000 nm. An IPCE as high as 33% is observed at 800 nm for MoS_2-coated Sb_2Se_3 in comparison with the 23% IPCE of a pristine Sb_2Se_3 sample (23%). The higher IPCE of MoS_2-coated Sb_2Se_3 at 800 nm is in response to its photocurrent density of $9.5\ mA\ cm^{-2}$ by integrating the IPCE spectra, which agrees with the photocurrent density from LSV
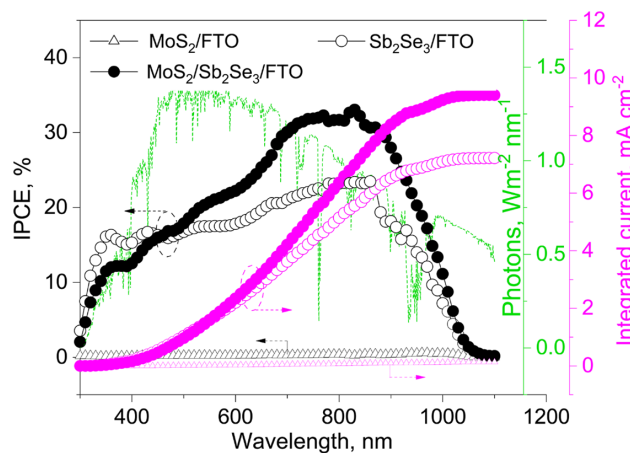
measurements (Figure 6c). The IPCE and integrated current for MoS_2 alone are very small, indicating little photoactivity from MoS_2 alone to contribute to the enhanced IPCE of the Sb_2Se_3/MoS_2 heterojunction, which allows a rapid charge separation at the Sb_2Se_3/MoS_2 interface upon light absorption to dramatically improve the photoconversion efficiency. Figure S8, Supporting Information, shows the current transient responses of pristine Sb_2Se_3 and MoS_2-coated Sb_2Se_3 photocathodes measured with chopped and steady illumination at 1 sun and a buffered 0.5 M Na_2SO_4 electrolyte at a constant potential of 0.2 V versus RHE. The photocurrent of as-grown Sb_2Se_3 degrades fast in the first 5 min and gradually becomes stable, whereas the photocurrent of MoS_2-coated Sb_2Se_3 shows rapid degradation in the first 10 min and gradually decreases until 1 h and stabilizes further. The MoS_2-coated Sb_2Se_3 NR arrays show higher photocurrent and durability, suggesting that MoS_2 can protect Sb_2Se_3 from photocorrosion. In the middle and end of the 2 h photostability measurement, the light was chopped "ON" and "OFF" to observe the photoactivity of the photocathodes. It is shown that the MoS_2-coated Sb_2Se_3 NR arrays possess a smaller dark current than that of the as-grown Sb_2Se_3, indicating that MoS_2 can effectively protect Sb_2Se_3.

3. Conclusions

In summary, we have demonstrated the scalable fabrication of sputter-deposited MoS_2 as an HER catalyst on the CSS-deposited Sb_2Se_3 NR array to form the core–shell structured MoS_2/Sb_2Se_3 NR array photocathodes. The PEC devices are suitable for water splitting with photocurrents as high as $-10\ mA\ cm^{-2}$ at $0\ V_{RHE}$ in a near-neutral (pH 6.5) buffered solution under simulated AM 1.5 solar illumination. The improved photocurrent generated in this core–shell structured MoS_2/Sb_2Se_3 NR arrays is associated with enhanced electronic carrier transport and light absorption by unique Q1D $(Sb_4Se_6)_n$ ribbons in the Sb_2Se_3 NR on the surface of the Sb_2Se_3 film. The thin sputtered MoS_2 layer on the Sb_2Se_3 NR arrays could effectively protect photocorrosion and further enhance carrier transport with the desired band

alignment. MoS_2 also catalyzes proton reduction to enhance the photocurrent response. This design of core–shell MoS_2/Sb_2Se_3 nanostructured photocathodes makes these types of low-dimensional antimony-based chalcogenides suitable for scale-up manufacturing for solar water-splitting applications.

4. Experimental Section

Deposition of Sb_2Se_3 Thin Films by CSS: The Sb_2Se_3 thin films (film thickness ≈1 μm) were deposited by a CSS system using high-purity Sb_2Se_3 powder (99.999%, Alfa Aesar) according to a previous report.[17] The transparent conducting FTO (TEC-15 NSG, US) was used as the substrate and was subsequently cleaned using detergent, acetone, isopropanol, and deionized water in the ultrasonic bath. Figure 1a shows the schematic process of the CSS deposition system, wherein the FTO substrate was held at the top of the AlN plate, and the appropriate amount of Sb_2Se_3 powder was placed at the bottom on the AlN plate. AlN plates with halogen lamps served as top and bottom heaters. The optimized condition for the growth of Sb_2Se_3 was as follows: the substrate temperature was held at 300 °C and Sb_2Se_3 powder temperature at 530 °C for 1 min with a chamber pressure of ≈10^{-2} Torr.

Deposition of MoS_2 Thin Films by Sputtering: MoS_2 thin films with thicknesses ranging from 20 to 50 nm were deposited by an RF magnetron sputtering system (AJA International, USA) using a 2 in. MoS_2 target (99.9% Kurt J. Lesker, USA) at room temperature with a target power of 50 W. The base pressure was 1×10^{-8} Torr, and the working pressure was 3×10^{-3} Torr with an Ar flow of 20 sccm. The thickness was controlled by sputtering deposition time.

Materials Characterization: The Sb_2Se_3 film thicknesses were estimated by a surface profilometer (Dektak II). The crystalline structures of the Sb_2Se_3 and MoS_2 and MoS_2-coated Sb_2Se_3 films were characterized using the X-ray diffractometer (X'Pert MPD, Philips, USA). The morphology and the chemical compositions of the films were analyzed using the SEM technique on a JEOL-7000 SEM machine equipped with EDS. High-resolution transmission electron microscopy (HRTEM) was performed using an FEI Tecnai F-20 TEM with scanning transmission electron microscopy, HAADF detector, and EDS. The Raman experiments were evaluated on a single-stage Raman spectrometer with a solid-state laser (Horiba LabRam HR, 532 nm wavelength). The absorbance and transmittance spectra were measured using a UV–vis spectrometer (Shimadzu UV-1800). AFM and EFM techniques were used to record the topography and surface charge distribution using an atomic force microscope (Park System XE70). AFM determined the thickness and surface roughness of the MoS_2 films. The XPS (Kratos, UK) was used to analyze the surface elemental composition and chemical states of the samples.

PEC Measurements: The PEC measurements were carried out using a standard three-electrode cell configuration, where a Pt wire was used as the counter electrode and a Ag/AgCl electrode as the reference electrode, in an electrochemical workstation (CHI760C, CH Instruments, USA). A near-neutral buffered 0.5 M Na_2SO_4 solution (pH ≈ 6.5) was used as the electrolyte. The sunlight was simulated using a commercial AM 1.5 G solar simulator (Newport Oriel, USA), which was calibrated to 1 sun (100 mW cm^{-2}) by a spectroradiometer. The incident photon-to-current conversion efficiency (IPCE) plots were obtained in the wavelength range of 300–1100 nm in a two-electrode structure, i.e., superstrate solar cells with the architecture FTO/Sb_2Se_3/MoS_2/graphite electrode using a quantum efficiency measurement system (EnliTech). EIS and M–S measurements were carried out using the same CHI76°c workstation, which was equipped with an electrochemical interface and impedance analyzer facility. The EIS plots were obtained in the alternating current (AC) frequency range of 0.01 Hz–100 kHz in the dark and light. The EIS data were fit with a suitable equivalent electrochemical circuit model. The M–S plots were recorded in the dark condition in the applied potential range from −0.6 to 0.1 V versus Ag/AgCl at 1 kHz frequency. The AC signal amplitude was 10 mV for both EIS and M–S measurements.

[1] N. M. Haegel, R. Margolis, T. Buonassisi, D. Feldman, A. Froitzheim, R. Garabedian, M. Green, S. Glunz, H.-M. Henning, B. Holder, I. Kaizuka, B. Kroposki, K. Matsubara, S. Niki, K. Sakurai, R. A. Schindler, W. Tumas, E. R. Weber, G. Wilson, M. Woodhouse, S. Kurtz, *Science* **2017**, *356*, 141.
[2] C. G. Morales-Guio, S. D. Tilley, H. Vrubel, M. Gratzel, X. Hu, *Nat. Commun.* **2014**, *5*, 3059.
[3] D. Bae, B. Seger, P. C. K. Vesborg, O. Hansen, I. Chorkendorff, *Chem. Soc. Rev.* **2017**, *46*, 1933.
[4] Y. Yu, Z. Zhang, X. Yin, A. Kvit, Q. Liao, Z. Kang, X. Yan, Y. Zhang, X. Wang, *Nat. Energy* **2017**, *2*, 17045.
[5] X. Cui, Z. Chen, Z. Wang, M. Chen, X. Guo, Z. Zhao, *ACS Appl. Energy Mater.* **2018**, *1*, 5822.
[6] J. L. Young, M. A. Steiner, H. Döscher, R. M. France, J. A. Turner, T. G. Deutsch, *Nat. Energy* **2017**, *2*, 17028.
[7] J. Joy, J. Mathew, S. C. George, *Int. J. Hydroge Energy* **2018**, *43*, 4804.
[8] D. Li, J. Shi, C. Li, *Small* **2018**, *14*, e1704179.
[9] H. Tateno, Y. Miseki, K. Sayama, *ChemElectroChem* **2017**, *4*, 3283.
[10] P. Zhang, L. Yu, X. W. Lou, *Angew. Chem., Int. Ed.* **2018**, *130*, 15296.
[11] C. G. Morales-Guio, L. Liardet, M. T. Mayer, S. D. Tilley, M. Grätzel, X. Hu, *Angew. Chem., Int. Ed.* **2015**, *127*, 674.
[12] J. R. Swierk, K. P. Regan, J. Jiang, G. W. Brudvig, C. A. Schmuttenmaer, *ACS Energy Lett.* **2016**, *1*, 603.
[13] J. Su, T. Minegishi, M. Katayama, K. Domen, *J. Mater. Chem. A* **2017**, *5*, 4486.
[14] B. Unveroglu, G. Zangari, *J. Electrochem. Soc.* **2019**, *166*, H3040.
[15] S. Mandati, B. V. Sarada, S. R. Dey, S. V. Joshi, *J. Power Sources* **2015**, *273*, 149.
[16] Z. Li, X. Liang, G. Li, H. Liu, H. Zhang, J. Guo, J. Chen, K. Shen, X. San, W. Yu, R. E. I. Schropp, Y. Mai, *Nat. Commun.* **2019**, *10*, 125.
[17] L. Guo, B. Zhang, Y. Qin, D. Li, L. Li, X. Qian, F. Yan, *Sol. RRL* **2018**, *2*, 1800128.

[18] J. Tan, W. Yang, Y. Oh, H. Lee, J. Park, R. Boppella, J. Kim, J. Moon, *Adv. Energy Mater.* **2019**, *9*, 1900179.

[19] J. Park, W. Yang, Y. Oh, J. Tan, H. Lee, R. Boppella, J. Moon, *ACS Energy Lett.* **2019**, *4*, 517.

[20] W. Yang, S. Lee, H.-C. Kwon, J. Tan, H. Lee, J. Park, Y. Oh, H. Choi, J. Moon, *ACS Nano* **2018**, *12*, 11088.

[21] Y. Zhou, L. Wang, S. Chen, S. Qin, X. Liu, J. Chen, D.-J. Xue, M. Luo, Y. Cao, Y. Cheng, E. H. Sargent, J. Tang, *Nat. Photonics* **2015**, *9*, 409.

[22] W. Yang, J. Ahn, Y. Oh, J. Tan, H. Lee, J. Park, H.-C. Kwon, J. Kim, W. Jo, J. Kim, J. Moon, *Adv. Energy Mater.* **2018**, *8*, 1702888.

[23] Y.-Q. Liu, M. Zhang, F.-X. Wang, G.-B. Pan, *J. Mater. Chem. C* **2014**, *2*, 240.

[24] Y. H. Kwon, M. Jeong, H. W. Do, J. Y. Lee, H. K. Cho, *Nanoscale* **2015**, *7*, 12913.

[25] J. Kim, W. Yang, Y. Oh, H. Lee, S. Lee, H. Shin, J. Kim, J. Moon, *J. Mater. Chem. A* **2017**, *5*, 2180.

[26] H. M. Chen, C. K. Chen, R. S. Liu, L. Zhang, J. Zhang, D. P. Wilkinson, *Chem. Soc. Rev.* **2012**, *41*, 5654.

[27] R. R. Prabhakar, W. Septina, S. Siol, T. Moehl, R. Wick-Joliat, S. D. Tilley, *J. Mater. Chem. A* **2017**, *5*, 23139.

[28] H. Lee, W. Yang, J. Tan, Y. Oh, J. Park, J. Moon, *ACS Energy Lett.* **2019**, *4*, 995.

[29] W. Yang, J. Moon, *J. Mater. Chem. A* **2019**, *7*, 20467.

[30] M. R. Gao, M. K. Chan, Y. Sun, *Nat. Commun.* **2015**, *6*, 7493.

[31] C. Ahn, J. Lee, H. U. Kim, H. Bark, M. Jeon, G. H. Ryu, Z. Lee, G. Y. Yeom, K. Kim, J. Jung, Y. Kim, C. Lee, T. Kim, *Adv. Mater.* **2015**, *27*, 5223.

[32] B. Y. Alfaifi, H. Ullah, S. Alfaifi, A. A. Tahir, T. K. Mallick, *Veruscript Funct. Nanomater.* **2018**, *2*, 1.

[33] L. A. King, W. Zhao, M. Chhowalla, D. J. Riley, G. Eda, *J. Mater. Chem. A* **2013**, *1*, 8935.

[34] P. S. Shinde, P. R. Fontenot, J. P. Donahue, J. L. Waters, P. Kung, L. E. McNamara, N. I. Hammer, A. Gupta, S. Pan, *J. Mater. Chem. A* **2018**, *6*, 9569.

[35] X. Yuan, H. Wang, J. Wang, G. Zeng, X. Chen, Z. Wu, L. Jiang, T. Xiong, J. Zhang, H. Wang, *Catal. Sci. Technol.* **2018**, *8*, 1545.

[36] J.-H. Huang, H.-H. Chen, P.-S. Liu, L.-S. Lu, C.-T. Wu, C.-T. Chou, Y.-J. Lee, L.-J. Li, W.-H. Chang, T.-H. Hou, *Mater. Res. Express* **2016**, *3*, 065007.

[37] R. Kaindl, B. C. Bayer, R. Resel, T. Muller, V. Skakalova, G. Habler, R. Abart, A. S. Cherevan, D. Eder, M. Blatter, F. Fischer, J. C. Meyer, D. K. Polyushkin, W. Waldhauser, *Beilstein J. Nanotechnol.* **2017**, *8*, 1115.

[38] A. Montgomery, L. Guo, C. Grice, R. A. Awni, S. Saurav, L. Li, Y. Yan, F. Yan, *Prog. Photovoltaics* **2019**, *27*, 665.

[39] L. Guo, B. Zhang, S. Ranjit, J. Wall, S. Saurav, A. J. Hauser, G. Xing, L. Li, X. Qian, F. Yan, *Sol. RRL* **2019**, *0*, 1900225.

[40] L. Guo, B. Zhang, S. Li, A. Montgomery, L. Li, G. Xing, Q. Zhang, X. Qian, F. Yan, *Mater. Today Phys.* **2019**, *10*, 100125.

[41] J. Major, Y. Y. Proskuryakov, K. Durose, *MRS Proc.* **2009**, *1165*, 1165.

[42] L.-N. Zhang, Z.-L. Lang, Y.-H. Wang, H.-Q. Tan, H.-Y. Zang, Z.-H. Kang, Y.-G. Li, *Energy Environ. Sci.* **2019**, *12*, 2569.

[43] M.-R. Gao, M. K. Y. Chan, Y. Sun, *Nat. Commun.* **2015**, *6*, 7493.

[44] X. Wen, C. Chen, S. Lu, K. Li, R. Kondrotas, Y. Zhao, W. Chen, L. Gao, C. Wang, J. Zhang, G. Niu, J. Tang, *Nat. Commun.* **2018**, *9*, 2179.

[45] C. Lee, H. Yan, L. E. Brus, T. F. Heinz, J. Hone, S. Ryu, *ACS Nano* **2010**, *4*, 2695.

[46] J. Yang, Y. Lai, Y. Fan, Y. Jiang, D. Tang, L. Jiang, F. Liu, J. Li, *RSC Adv.* **2015**, *5*, 85592.

[47] J. Tan, W. Yang, Y. Oh, H. Lee, J. Park, J. Moon, *ACS Appl. Mater. Interfaces* **2018**, *10*, 10898.

[48] X. Liu, C. Chen, L. Wang, J. Zhong, M. Luo, J. Chen, D.-J. Xue, D. Li, Y. Zhou, J. Tang, *Prog. Photovoltaics* **2015**, *23*, 1828.